

Measuring the Resolved Star Formation Main Sequence in TNG100: Fitting Technique MattersBRYANNE McDONOUGH ^{1,2} OLIVIA CURTIS ^{3,2} AND TEREASA G. BRAINERD ²¹*Department of Physics, Northeastern University, 360 Huntington Ave, Boston, MA, USA*²*Institute for Astrophysical Research, Boston University, 725 Commonwealth Ave, Boston, MA, USA*³*Department of Astronomy & Astrophysics, The Pennsylvania State University, 251 Pollock Road, University Park, PA, USA*

ABSTRACT

The resolved star formation main sequence (rSFMS) and similar spatially resolved scaling relationships are frequently measured in both observed and simulated data. However, comparisons of these measurements are hindered by various differences between studies such as spatial resolution, sample selection criteria, and fitting technique. Using maps of Σ_* and Σ_{SFR} derived using simulated galaxies from TNG100, we investigate the dependence of rSFMS measurements on spatial resolution, smoothing scale, and fitting technique. When the ridge line of the rSFMS is fit with a double linear function, we find that the slope of the rSFMS at low- Σ_* is independent (within 2σ) of spatial resolution and smoothing scale. We demonstrate that this method offers significant benefits over fitting the rSFMS with a single linear function using ordinary least squares.

Keywords: star formation (1569), astronomical simulations (1857), galaxy evolution (594), scaling relations (2031), galaxy properties (615)

1. INTRODUCTION

Scaling relationships are strong correlations between galaxy properties that arise due to the physical mechanisms that drive galaxy evolution. In particular, at low redshifts there exist relationships between the surface densities of gas mass, stellar mass (Σ_*), and star formation rate (Σ_{SFR}) on sub-kiloparsec scales. These relationships are inherently linked to the evolution of galaxies, as they describe the formation of stellar populations. The relationship between Σ_* and Σ_{SFR} is often called the resolved star formation main sequence (rSFMS; e.g., [Cano-Díaz et al. 2016](#); [Maragkoudakis et al. 2016](#); [Abdurro'uf & Akiyama 2017](#); [Liu et al. 2018](#); [Trayford & Schaye 2019](#); [Erroz-Ferrer et al. 2019](#); [Medling et al. 2018](#); [Lin et al. 2019](#); [Bluck et al. 2020a](#); [Pessa et al. 2021](#)) and is the focus of this *Letter*.

Scaling relationships play an important role in cosmological hydrodynamic simulations of galaxy evolution and unconstrained parameters can be calibrated to reproduce select relationships. For example, the IllustrisTNG simulations (Nelson et al. 2018; Pillepich et al. 2018; Springel et al. 2018; Naiman et al. 2018; Marinacci et al. 2018; Nelson et al. 2019) were calibrated to reproduce the stellar-to-halo mass, stellar mass – stellar size, and black hole – galaxy mass relations. Relationships that are not used to calibrate a simulation can, instead, be used to validate it. For example, in McDonough et al. (2023) we showed that the 100–Mpc box of the IllustrisTNG suite (TNG100) broadly reproduced the rSFMS with a slope in agreement with that found by (Bluck et al. 2020a) for MaNGA (Bundy et al. 2015) galaxies.

As both simulations and observations improve in resolution and complexity, a need for accurate and unbiased quantitative comparisons arises. Unfortunately, differences in galaxy sample selection, spatial resolution, pre-selection of star-forming regions, star formation timescales, and techniques for measuring scaling relationships have made such comparisons challenging. The slopes of the rSFMS presented in the literature range from ~ 0.5 to ~ 1 , with reported confidence intervals ranging from $\sim 0.0002 - 0.2$ (e.g., Cano-Díaz et al. 2016; Maragkoudakis et al. 2016; Abdurro’uf & Akiyama 2017; Liu et al. 2018; Trayford & Schaye 2019; Erroz-Ferrer et al. 2019; Bluck et al. 2020a; Hani et al. 2020; Pessa et al. 2021; McDonough et al. 2023). Using spatially resolved maps of simulated galaxies from the FIRE project (Wetzel et al. 2023), Hani et al. (2020) found that the rSFMS slope depends on the fitting method, star formation timescales, and spatial resolution.

The rSFMS is likely a byproduct of two more fundamental relations (e.g., Baker et al. 2023): the molecular gas main sequence (i.e., $\Sigma_{H_2} - \Sigma_*$) and the Kennicutt-Schmidt relation (i.e., $\Sigma_{H_2} - \Sigma_{\text{SFR}}$). However, the rSFMS remains useful as a proxy for the more fundamental relations due to the challenges associated with obtaining molecular gas measurements for large observational samples (i.e., the need for millimeter wavelengths). Even in simulation space, the rSFMS requires only the analysis of stellar particles, while investigations of the other relations would require analysis of both stellar and gas particles. Thus, a consistent measurement of the rSFMS slope is desirable for validation of simulation results and for probing the physics that drive star formation. Further, a consistent method for measuring the rSFMS relation should also be applicable to the more fundamental scaling relations.

Many studies in the literature use some variation of ordinary least squares (OLS) to fit a line to their samples of spectral pixels (i.e., spaxels). Typically, some criteria are used to pre-select star-forming spaxels and a line is then fit to either the full sample or the median of the sample in bins of stellar mass. This method is not ideal because spaxels are not normally distributed about the rSFMS; as regions of galaxies quench, the SFR of spaxels will decrease while stellar mass remains roughly fixed. The introduction of pre-selection criteria for star-forming spaxels mitigates this issue to some degree, but is hard to apply consistently across studies, especially those using different SFR tracers.

Renzini & Peng (2015) describe an objective definition for the global star-forming main sequence (SFMS; i.e., $M_* - \text{SFR}$ relationship) based on the “ridge line” of data in 3D $M_* - \text{SFR}$ plots. The ridge line method works by fitting a line to the mode of Σ_{SFR} in bins of Σ_* . This method is intended to ameliorate biases introduced by the presence of quenching spaxels without pre-selecting star-forming systems. The ridge line method has been adopted to measure the rSFMS in both observations (Abdurro’uf & Akiyama 2017; Bluck et al. 2020a) and simulations (McDonough et al. 2023).

In this letter, we investigate how different methodologies for obtaining maps of Σ_* and Σ_{SFR} from galaxies in the TNG100 simulation affect the resulting rSFMS. We demonstrate that these effects are minimized when the slope is obtained by fitting a double linear function to the ridge line. In Section 2, we discuss the TNG simulations and our methodology for obtaining spatially-resolved data. In Section 3, we present our results for rSFMS fits obtained with: [i] different fitting techniques, [ii] spatially-resolved maps that have different resolutions, and [iii] different adaptive smoothing scales. In Section 4, we summarize our results and present our prescription for measuring unbiased, objective rSFMS slopes. To ensure the reproducibility of this work, the data and Jupyter notebook containing the analysis software is preserved on Zenodo: [doi: 10.5281/zenodo.15047581284](https://doi.org/10.5281/zenodo.15047581284).

2. DATA AND METHODS

Our galaxy sample is identical to that of McDonough et al. (2023) and McDonough et al. (2025), and was drawn from the TNG100 simulation. TNG100 used the IllustrisTNG model of galaxy formation, which adopted a Planck Collaboration (2016) cosmology. TNG100 has a comoving box length of $75h^{-1}\text{Mpc}$ and a target baryonic particle mass of $\sim 10^6 h^{-1} M_\odot$. The IllustrisTNG model was calibrated such that at $z = 0$ it reproduces the observed stellar mass function, the total gas mass of massive groups, and the following relations: stellar-to-halo mass, stellar mass to stellar size, and black hole to galaxy mass (Pillepich et al. 2018). Additionally, the model was calibrated to reproduce the shape of the cosmic star formation rate density as a function of redshift out to $z = 10$.

Our galaxy sample selection criteria are described in full in McDonough et al. (2023) and here we provide only a brief summary. Specifically, we ensure sufficient spatial resolution by limiting our sample to galaxies with $R_e > 4$ kpc and more than 1000 stellar particles within $2R_e$, where R_e is the r -band half-light radius. We obtain galaxy magnitudes and radii from the SDSS Photometry, Colors, and Mock Fiber Spectra (Nelson et al. 2018) and Stellar Projected Sizes (Genel et al. 2018) catalogs, respectively. These criteria result in a sample of 6197 TNG100 galaxies, including centrals and satellites. We compute time-averaged SFRs using stellar particles formed in the last 20 and 100 Myrs. Unlike McDonough et al. (2023), here we do not include spaxels for which no stellar particles were formed in the last 100 Myrs. These are comparable to observational spaxels where a measurement of SFR cannot be made due to poor signal-to-noise.

As in [McDonough et al. \(2023\)](#), we obtain spatially-resolved maps of stellar mass and SFR using a cubic spline kernel to project stellar particles onto a 2D plane that corresponds to a face-on projection of the galaxy. The 2D cubic spline kernel is:

$$W(r, h_{sml}) = \frac{40}{7\pi} \frac{1}{h_{sml}^2} \begin{cases} 1 - 6q^2 + 6q^3 & \text{if } 0 \leq q \leq \frac{1}{2}, \\ 2(1 - q)^3 & \text{if } \frac{1}{2} < q \leq 1, \\ 0 & \text{if } q > 1, \end{cases} \quad (1)$$

where r is the radius a particle is smoothed over, h_{sml} is the distance between a particle and its N th nearest neighbor, and $q \equiv r/h_{sml}$. In [McDonough et al. \(2023\)](#), we presented our fiducial results for the rSFMS using 2D maps with a spatial resolution of $500h^{-1}\text{pc}$ (~ 750 pc) and a value of $N = 64$ for the cubic spline kernel. Here, we obtain results from maps with different spatial resolutions and different values of N . Using $N = 64$ we construct maps with spatial resolutions of 500 pc, ~ 750 pc, 1 kpc, and ~ 1.5 kpc. At a spatial resolution of ~ 750 pc, we also construct maps using $N = 8, 16, 24, 32,$ and 64. Pixels in 2D maps of galaxies from data obtained with integral field spectroscopy (IFS) are often referred to as spectral pixels or ‘spaxels.’ While the pixels in our 2D maps are not true spaxels, we refer to them as such for the sake of clarity.

In [Section 3.1](#), we present the rSFMS slope that we obtain using different methods to fit spatially resolved data. The rSFMS slope is often obtained from a fit to a single linear function (in logarithmic space). However, several studies have found that there is a point at which the global SFMS turns over (e.g., [Renzini & Peng 2015](#); [Popesso et al. 2019](#); [Mancini et al. 2019](#)), and the bend also appears in the rSFMS (e.g., [McDonough et al. 2023](#)). Any fits made to a single linear function are either biased by the rSFMS turnover or must pre-select the regime where the rSFMS is purely linear.

Although we mainly fit the ridge line to a double linear function to identify the rSFMS, we compare results for the rSFMS slope using variations of OLS fits in [§3.1](#). For the non-OLS fits, we use the open-source `ScaleRPy`¹ ([McDonough 2025](#)) Python package to identify and fit the ridge line. In each bin of Σ_* , we use a Gaussian kernel density estimator (KDE; e.g., [Scott 1992](#)) to identify the mode of Σ_{SFR} . The ridge of our data is defined as the collection of points that correspond to the centers of the Σ_* bins and the mode of the KDE of Σ_{SFR} in those bins. The ridge line and fits are computed over $10^6 < \Sigma_* / [M_\odot \text{kpc}^2] < 10^9$, where there is sufficient data to obtain a KDE for each mass bin. The ridge

¹ <https://github.com/bryannemcd/ScaleRPy>

line is fit with a double linear function parameterized as:

$$\log_{10} \Sigma_{\text{SFR,MS}} = \begin{cases} \gamma \log_{10} \Sigma_* + y_0 & \text{if } \Sigma_* < \Sigma_*^{\text{to}}, \\ \gamma' \log_{10} \Sigma_* + y'_0 & \text{if } \Sigma_* > \Sigma_*^{\text{to}}, \end{cases} \quad (2)$$

where γ is the rSFMS slope, y_0 is the y-axis zero point, γ' is the slope of the high-mass end of the rSFMS, Σ_*^{to} is the value of Σ_* where the main sequence turns over, and $y'_0 \equiv (\gamma - \gamma') \log_{10} \Sigma_*^{\text{to}} + y_0$.

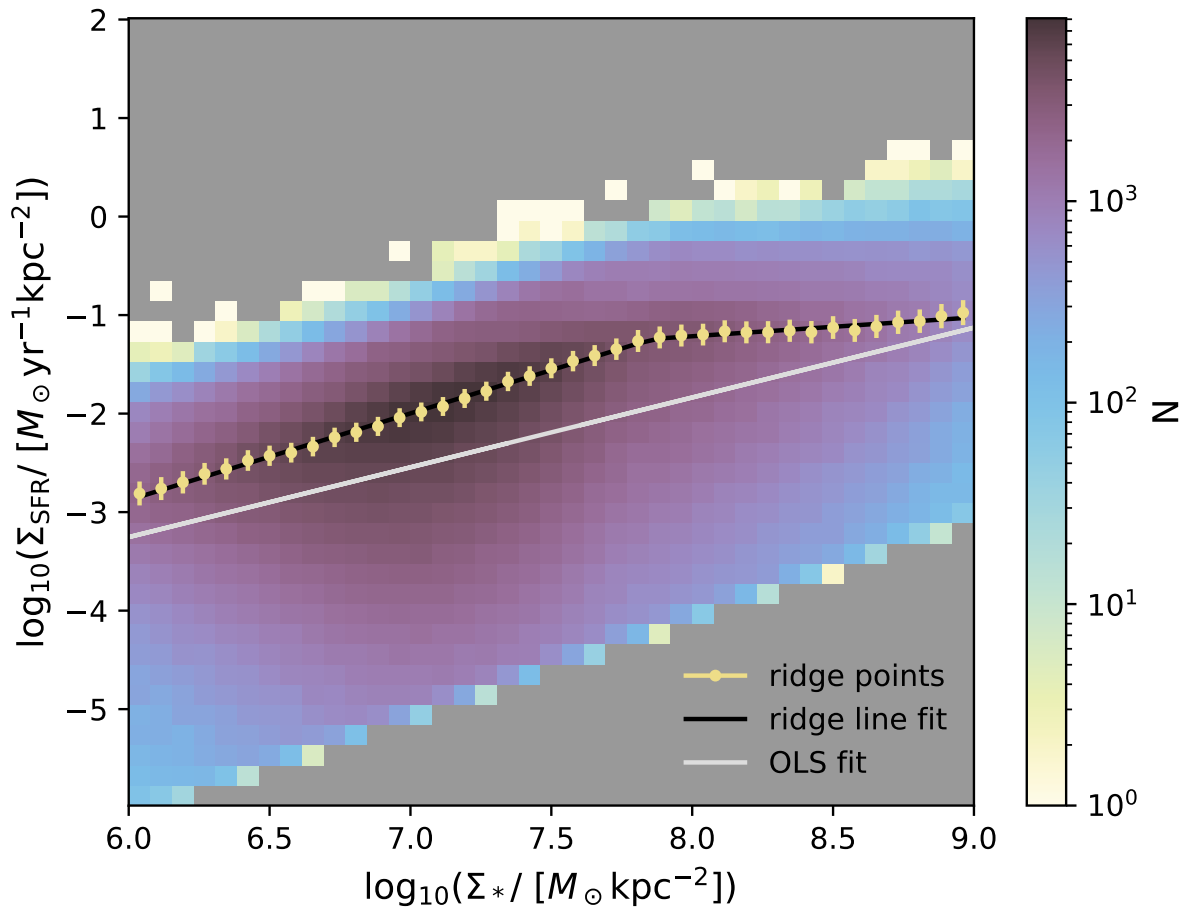


Figure 1. An example of the rSFMS from our fiducial maps, which demonstrates the ridge line and ordinary least squares fitting techniques. The 2D histogram shows the number of spaxels in bins of Σ_* and Σ_{SFR} . Yellow points indicate the ‘ridge’ or mode of the data in bins of Σ_* , and the black line shows the double linear fit to those ridges. The grey line shows the fit to a single linear function obtained using OLS and the full data set.

In Figure 1, we compare the fits obtained with OLS (grey) and the ridge line (black) methods for the distribution of Σ_* - Σ_{SFR} from our fiducial maps. The yellow points indicate the ridges in each bin of Σ_* . For consistency with other investigations, we fit a single linear function with OLS (gray). However, the method we present here fits a double

Table 1. Parameters of fits to the $z = 0$ resolved star formation main sequence recovered from maps of TNG100 galaxies generated with different methods.

Name	Resolution (pc)	N	γ	y_0	γ'	Σ_*^{to}	R^2
fid-OLS	~ 0.75 kpc	64	0.71 ± 0.01	-7.51 ± 0.01	N/A	N/A	0.2168
fid-OLSdoub	~ 0.75 kpc	64	0.52 ± 0.01	-6.27 ± 0.06	0.73 ± 0.01	6.64 ± 0.02	0.2173
fiducial	~ 0.75 kpc	64	0.88 ± 0.01	-8.15 ± 0.07	0.19 ± 0.02	7.86 ± 0.02	0.9983
N32	~ 0.75 kpc	32	0.90 ± 0.01	-8.07 ± 0.08	0.16 ± 0.01	7.58 ± 0.02	0.9979
N24	~ 0.75 kpc	24	0.91 ± 0.01	-8.07 ± 0.08	0.16 ± 0.01	7.58 ± 0.02	0.9979
N16	~ 0.75 kpc	16	0.91 ± 0.02	-8.0 ± 0.1	0.15 ± 0.01	7.32 ± 0.02	0.9974
N8	~ 0.75 kpc	8	0.86 ± 0.02	-7.4 ± 0.2	0.13 ± 0.01	7.12 ± 0.02	0.9952
res500	0.5 kpc	64	0.86 ± 0.01	-8.02 ± 0.06	0.12 ± 0.05	8.25 ± 0.03	0.9982
res1000	1 kpc	64	0.86 ± 0.03	-8.0 ± 0.2	0.31 ± 0.03	7.50 ± 0.07	0.9866
res1500	~ 1.5 kpc	64	0.86 ± 0.1	-8.1 ± 0.7	0.42 ± 0.04	7.0 ± 0.2	0.9552

NOTE—Fits are done with the ridge line method except for the fid-OLS and fid-OLSdoub cases.

linear function to the ridge line (black) to account for the turnover in the rSFMS. Throughout, we use the R^2 statistic, also known as the coefficient of determination, to measure the goodness of our fits. A value of $R^2 = 1$ means that the model fits the data perfectly.

3. RESULTS

3.1. Fitting Method

For comparison with other results in the literature, we have performed two OLS fits to star-forming spaxels in our sample of TNG100 galaxies. The first (which we will refer to as fid-OLS) is performed over the same range of stellar masses as the other cases ($10^6 < \Sigma_* / [M_\odot \text{kpc}^2] < 10^9$) and is fit with a single linear function. The fid-OLS fit is represented by the gray line in Figure 1. We also use OLS to fit a double linear function to the full sample of spaxels (fid-OLSdoub) for better comparison to the fits we perform with the ridge line technique. Results for the fits to the rSFMS for our different maps of TNG100 galaxies are summarized in Table 1.

From Table 1, when the rSFMS is fit with a single line, the fid-OLS fit returns a slope that is significantly shallower than those obtained with the ridge line method. The slope obtained with the ridge line method for the fiducial maps is $\gamma = 0.88 \pm 0.01$, while the slope of the fid-OLS case is $\gamma = 0.71 \pm 0.01$. The fid-OLSdoub case is interesting because the slope at the low-mass end ($\gamma = 0.52 \pm 0.01$) is shallower than the slope at the high-mass end ($\gamma' = 0.73 \pm 0.01$), which is at odds with the other results in Table 1.

The significant differences between the OLS fits and the ridge line fit are unsurprising. The main advantage of the ridge line method is that it is not biased by the presence of spaxels transitioning off the main sequence. This transition is expected due to the natural evolution of galaxies.

The R^2 statistic shows that the OLS models do a poor job of describing the variation of Σ_{SFR} with Σ_* . For the fid-OLS and fid-OLSDoub cases, $R^2 = 0.2168$ and 0.2173 , respectively. However, with $R^2 = 0.9983 \approx 1$, the ridge line method results in a model that fits the data well. Although it may be possible to improve R^2 for the OLS cases by imposing additional criteria to limit the sample to spaxels that are actively star-forming, this would defeat the goal of obtaining an objective and broadly comparable rSFMS slope.

In the following subsections, we fit the rSFMS with a double linear function using the ridge line method.

3.2. Spaxel Resolution

In Figure 2, we present the ridge lines derived from maps with different spatial resolutions (left) and different numbers of nearest neighbors for the smoothing radius (right).

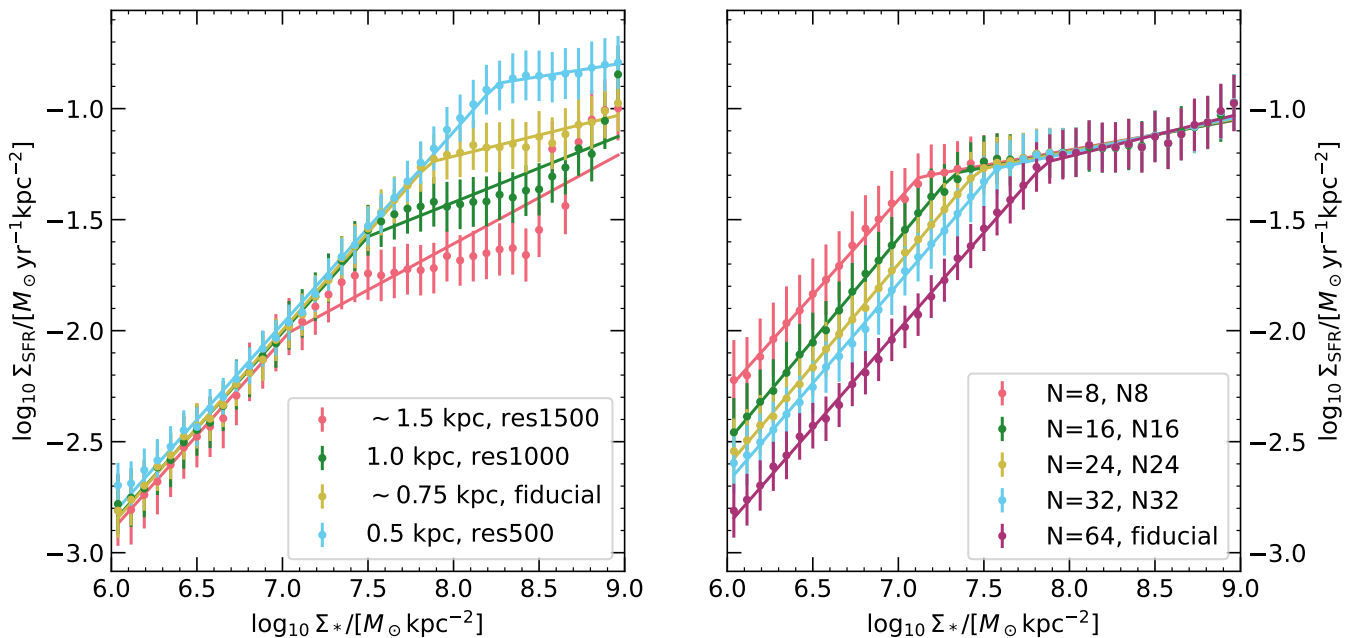


Figure 2. Comparison of the modes of spaxels in the star-forming portion of the $\Sigma_* - \Sigma_{\text{SFR}}$ diagram derived from maps with different spatial resolutions (left) and different smoothing scales (right). Points represent the ridges identified in each bin of Σ_* and lines of the same color represent the fit to those ridges. Error bars are approximated as the KDE bandwidth estimated via Scott’s rule.

Previous results (Hani et al. 2020) have indicated that the spatial resolution of the surface density maps may affect the slope obtained for the rSFMS. In Figure 2 (left), we plot the ridge lines from the 2D distribution in the $\Sigma_* - \Sigma_{\text{SFR}}$ diagram of star-forming spaxels taken from maps with the following spaxel resolutions: blue: 0.5kpc ($\sim 0.34h^{-1}\text{kpc}$), yellow: $\sim 0.74\text{kpc}$ ($0.5h^{-1}\text{kpc}$), green: 1kpc ($\approx 0.68h^{-1}\text{kpc}$), pink: $\sim 1.5\text{kpc}$ ($1h^{-1}\text{kpc}$). Points show the ‘ridge line’ or modes of the distribution of Σ_{SFR} in bins of Σ_* , while the solid lines show the fits to the ridge lines. Altering the resolution of the maps affects the surface mass at which the main sequence turns over, but the slopes at the low-mass end agree within 1σ at all resolutions (see Table 1).

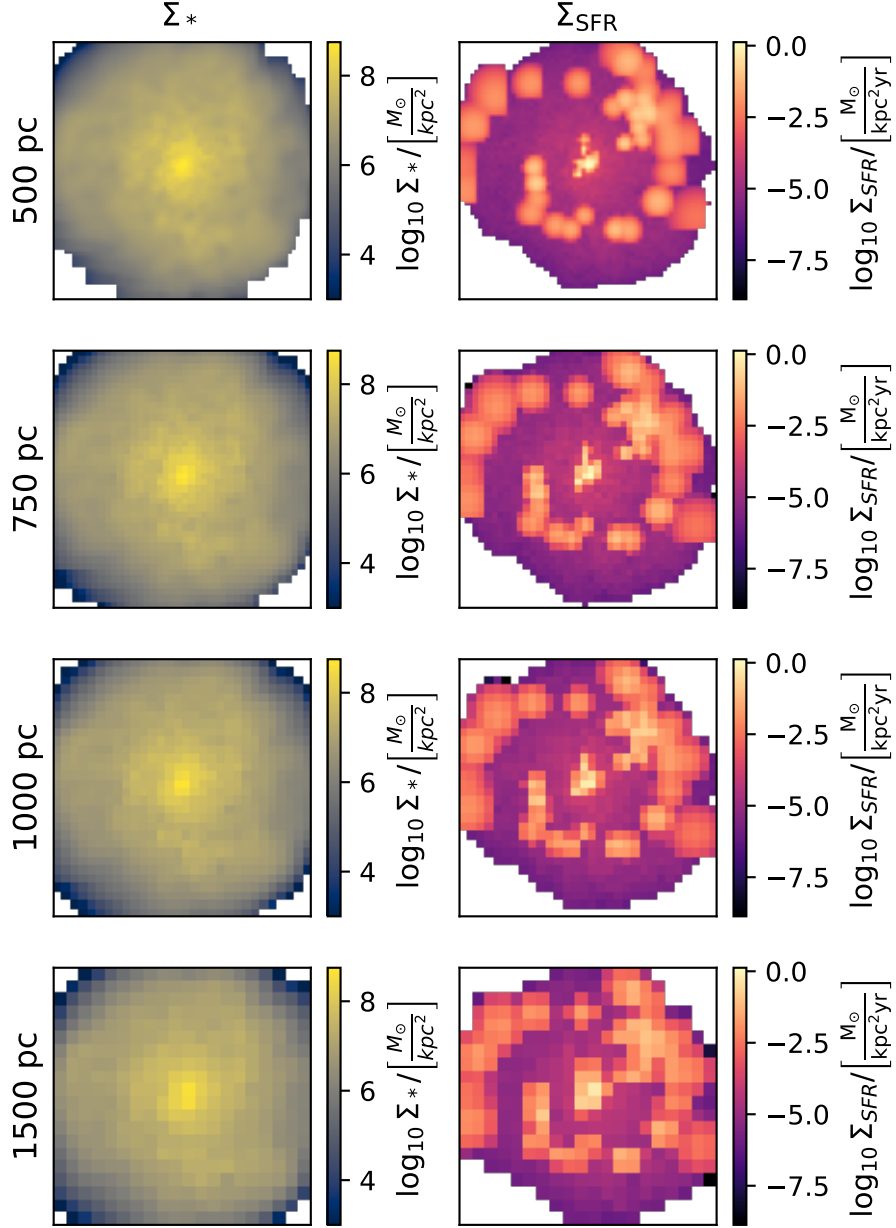


Figure 3. Maps of Σ_* (left) and Σ_{SFR} (right) for TNG100-99-540858. Each row contains maps generated at different spaxel resolutions, as indicated on the left.

As the spaxel size decreases, the rSFMS turns over at higher values of Σ_* . Due to the large number of contributing stellar particles and relatively large smoothing radius ($N = 64$), the stellar mass surface density should remain relatively constant with spaxel size. However, the sparser sampling of stellar particles contributing to Σ_{SFR} leads to concentrated star formation regions being spread over larger spaxels at lower resolutions, resulting in lower SFR surface densities.

Figure 3 illustrates the effects of spatial resolution on maps of Σ_* and Σ_{SFR} for a particular TNG100 galaxy, TNG100-99-540858². TNG100-99-540858 is a main-sequence, central galaxy with a stellar mass of $6.4 \times 10^9 M_\odot$. The central star-forming region seen in Figure 3 is spread over a larger area at lower resolutions. This effect contributes to the trend observed in Figure 2 (left).

From Table 1, the value of R^2 decreases from the fiducial value ($R^2 = 0.9983$) for the res1000 and res1500 cases, which have $R^2 = 0.9866$ and 0.9552 , respectively. This is likely due to the large variation in the ridge line at high masses, which we attribute to a reduction in the number of high- Σ_* spaxels in these cases. This reduction is a result of there being fewer spaxels in low-resolution maps and that these spaxels have higher surface areas.

3.3. Adaptive Smoothing Scale

Equation 1 describes how simulated stellar particles are smoothed onto a grid of spaxels to determine spatially resolved star formation rates. In this equation, particles are smoothed over a radius of h_{smi} which is defined as the distance of a particle to its N^{th} nearest neighbor. In Figure 2 (right), we present the rSFMS ridge line that results from maps generated with $N = 8$ (pink), 16 (green), 24 (yellow), 32 (blue), and 64 (purple). From Table 1, the rSFMS slopes agree within 2σ for all values of N explored here. However, for $\Sigma_* < \Sigma_*^{\text{to}}$, the modes are offset such that as N increases, the zero point decreases. For $\Sigma_* > \Sigma_*^{\text{to}}$, all cases turn over at $\sim \Sigma_{\text{SFR}} \sim 10^{-1.25} M_\odot \text{yr}^{-1} \text{kpc}^{-2}$, but the turnover occurs at higher Σ_* due to the offset in normalization.

Figure 4 illustrates the effects of smoothing scale on maps of Σ_* and Σ_{SFR} for the galaxy shown Figure 3. For small N values, the maps become patchier, while the typical size of a star-forming region in the right column becomes smaller.

As N decreases, the radius over which a stellar particle is smoothed decreases. Unlike the cases in which resolution is varied, this affects both the measurements of Σ_* (determined via the distribution of all stellar particles) and Σ_{SFR} (determined via the distribution of recently formed stellar particles). Thus, it is difficult to discern why altering N has the effect seen in Figure 2 (right). However, the general trend of increasing Σ_{SFR} with decreasing N can be explained by the concentration of stellar particles that contribute to star formation when smoothed over smaller radii. That is, higher values of Σ_{SFR} are obtained when young stellar particles are smoothed over fewer spaxels.

4. SUMMARY & DISCUSSION

In this *Letter*, we compared ridge line fits of the rSFMS obtained with `ScaleRPy` from maps of TNG100 galaxies generated at different spatial resolutions and with different smoothing scales. We find that the ridge line of the rSFMS is fit well by a double linear function (in log space). At the low-mass end, the slopes we obtain with the ridge line

² This identifier indicates that this galaxy is from the 99th snapshot of TNG100, and is indexed as 540858 in the subhalo catalog.

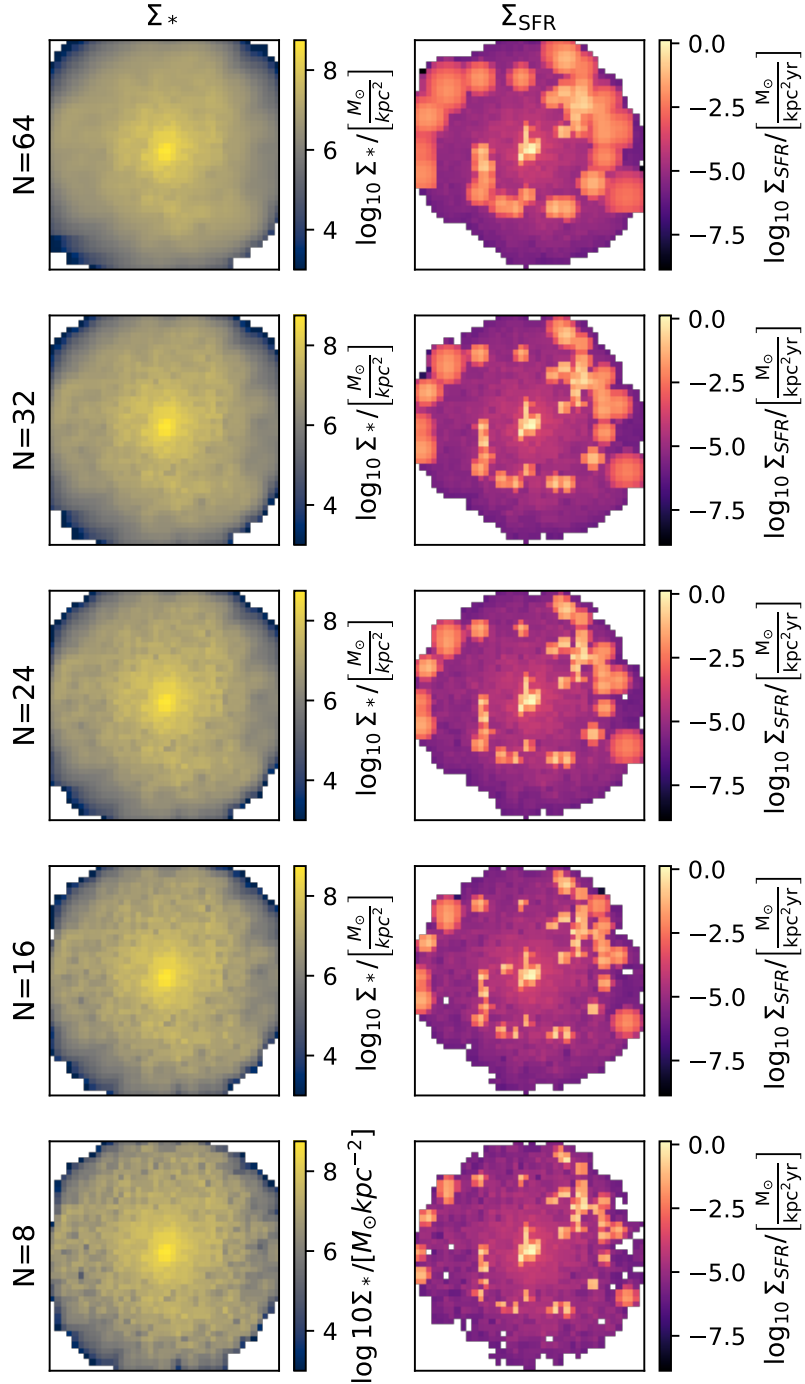


Figure 4. Maps of Σ_* (left) and Σ_{SFR} (right) for TNG100-99-540858. Each row contains maps generated with different values of N , as indicated on the left.

method agree with each other within 2σ in almost all cases. The only exception is the res500 case, where the low-mass slope agrees with all others only at 3σ .³ We find that the stellar mass surface density at which the rSFMS turns over

³ We note that a resolution of 500 pc is close to the spatial resolution limit of TNG100, which has a gravitational softening length of ~ 180 pc.

(Σ_*^{to}) becomes larger at larger smoothing scales and at finer spatial resolutions. While the normalization of Σ_{SFR} at the low-mass end (y_0) is identical within 1σ for different spatial resolutions, y_0 decreases with increasing values of N . The rSFMS plateaus at increasing values of Σ_{SFR} as spatial resolution becomes finer, but plateaus at roughly the same value of Σ_{SFR} across varying smoothing scales.

The cases we present here demonstrate that there are significant differences in the rSFMS from maps generated at different spatial resolutions and with different smoothing scales, particularly at the high-mass end. However, we demonstrate that there is a remarkable consistency in the slope at the low-mass end (γ). By fitting a double linear function to the ridge line of the rSFMS, we are able to parameterize the differences at the high-mass end, while obtaining an objective slope for the low-mass end of this distribution. Thus, the slope of the low-mass end of the rSFMS obtained with our method is well-suited for comparing this relationship in spatially resolved data obtained with a variety of methods.

As the rSFMS is often fit with OLS and a single linear function in the literature, we fit ‘spaxels’ from our fiducial maps of TNG100 galaxies with OLS. Whether or not we limit the OLS fit to spaxels within the regime where the rSFMS can be approximated as a single linear function, the slope we obtain is significantly lower than the slopes obtained with the ridge line method. This is because the spaxels are not normally-distributed about the main sequence, and spaxels that are actively quenching will bias the distribution toward lower values of Σ_{SFR} at higher masses. To obtain reasonable slopes with the OLS method, the fits are often limited to spaxels that are actively star-forming and are within the regime where the rSFMS appears linear. In contrast, the ridge line method does not require pre-selection of star-forming spaxels and only requires limiting the fit to stellar masses where there is enough data to obtain a good kernel density estimate. Thus, the ridge line method allows for the inclusion of more spaxels than the OLS method and does not assume the turnover mass, resulting in a more objective measurement of the slope. This is especially desirable when comparing the rSFMS slope obtained from different observations and simulations, where spatial resolution and sample selection criteria may differ.

Hani et al. (2020) explored the dependence of the rSFMS slope on spatial resolution for galaxies from the FIRE project. They fit the rSFMS with a single linear function and found that the slope became steeper as spatial resolution decreased. While we find that the rSFMS slope at low masses (γ) is roughly constant with changing spatial resolution, we find that the slope at high masses (γ') becomes steeper as spatial resolution decreases. The ‘spaxel’ samples used by Hani et al. (2020) appear to be biased toward stellar masses greater than the turnover masses we have identified (Σ_*^{to}), which means the slopes they obtained would be biased toward the high-mass end of the relation. Thus, we find that our results are consistent with those of Hani et al. (2020). This further demonstrates the benefits of fitting the rSFMS with a double linear function. Pessa et al. (2021) fit the rSFMS, resolved molecular gas main sequence,

and Kennicutt-Schmidt relation with a single line and found that the slopes were independent of spatial resolution in a spaxel sample drawn from the Physics at High Angular resolutions in Nearby Galaxies (PHANGS) survey (Leroy et al. 2021). For all three relations, the PHANGS data appear to deviate from linearity at high surface mass densities, although this seems to introduce only a small bias in the slopes obtained with their methodology.

In our efforts to obtain comparable, objective measurements of the rSFMS slope, we have tried to eliminate subjective choices such as imposing bounds on the fit. However, we found it necessary to impose an upper limit on Σ_* , where the identified ridge points are no longer well described by a double linear function. This may be due in part to the relative sparseness of high surface mass density spaxels, resulting from the poor sampling of very high-mass galaxies in the limited volume of TNG100. The advantage of fitting a double linear function is that the slope at the low-mass end (γ) is not biased by our imposed upper limit. However, this is not the case for the slope at the high-mass end (γ'). It is not clear whether the high-mass end of the rSFMS is best described by a linear function, or what causes the change in slope at Σ_*^{to} . Our results indicate that the location of the turnover point depends at least in part on spatial resolution and the sizes of star-forming regions. Further research will be necessary to understand and constrain the shape of the high-mass end of this distribution and the location of the turnover point.

In conclusion, we find that the slope at the low-mass end of the rSFMS is independent of spatial resolution and smoothing scale when it is measured using a double linear fit to the ridge line of the data. Additionally, this method does not require pre-selection of star-forming spaxels and parameterizes the location at which the rSFMS slope turns over. Thus, this is a promising method for making measurements of scaling relationships that can be compared across studies. The open-source `ScaleRPy` package facilitates the adoption of the method presented here for both global and resolved scaling relations.

1 We would like to acknowledge the work and documentation provided by the IllustrisTNG team that has made this
 2 paper possible. The IllustrisTNG simulations were undertaken with compute time awarded by the Gauss Centre
 3 for Supercomputing (GCS) under GCS Large-Scale Projects GCS-ILLU and GCS-DWAR on the GCS share of the
 4 supercomputer Hazel Hen at the High Performance Computing Center Stuttgart (HLRS), as well as on the machines of
 5 the Max Planck Computing and Data Facility (MPCDF) in Garching, Germany. The additional computational work
 6 done for this paper was performed on the Shared Computing Cluster which is administered by Boston University's
 7 Research Computing Services. This work was partially supported by NSF grant AST-2009397. BM acknowledges
 8 support by Northeastern University's Future Faculty Postdoctoral Fellowship Program.

Software: SciPy (Virtanen et al. 2020); ScaleRPy (McDonough 2025)

REFERENCES

- Abdurro'uf, & Akiyama, M. 2017, *MNRAS*, 469, 2806, doi: [10.1093/mnras/stx936](https://doi.org/10.1093/mnras/stx936)
- Baker, W. M., Maiolino, R., Belfiore, F., et al. 2023, *MNRAS*, 518, 4767, doi: [10.1093/mnras/stac3413](https://doi.org/10.1093/mnras/stac3413)
- Bluck, A. F. L., Maiolino, R., Sánchez, S. F., et al. 2020a, *MNRAS*, 492, 96, doi: [10.1093/mnras/stz3264](https://doi.org/10.1093/mnras/stz3264)
- Bundy, K., Bershadsky, M. A., Law, D. R., et al. 2015, *ApJ*, 798, 7, doi: [10.1088/0004-637X/798/1/7](https://doi.org/10.1088/0004-637X/798/1/7)
- Cano-Díaz, M., Sánchez, S. F., Zibetti, S., et al. 2016, *ApJL*, 821, L26, doi: [10.3847/2041-8205/821/2/L26](https://doi.org/10.3847/2041-8205/821/2/L26)
- Erroz-Ferrer, S., Carollo, C. M., den Brok, M., et al. 2019, *MNRAS*, 484, 5009, doi: [10.1093/mnras/stz194](https://doi.org/10.1093/mnras/stz194)
- Genel, S., Nelson, D., Pillepich, A., et al. 2018, *MNRAS*, 474, 3976, doi: [10.1093/mnras/stx3078](https://doi.org/10.1093/mnras/stx3078)
- Hani, M. H., Hayward, C. C., Orr, M. E., et al. 2020, *MNRAS: Letters*, 493, L87, doi: [10.1093/mnrasl/slaa013](https://doi.org/10.1093/mnrasl/slaa013)
- Leroy, A. K., Hughes, A., Liu, D., et al. 2021, *ApJS*, 255, 19, doi: [10.3847/1538-4365/abec80](https://doi.org/10.3847/1538-4365/abec80)
- Lin, L., Pan, H.-A., Ellison, S. L., et al. 2019, *ApJL*, 884, L33, doi: [10.3847/2041-8213/ab4815](https://doi.org/10.3847/2041-8213/ab4815)
- Liu, Q., Wang, E., Lin, Z., et al. 2018, *The Astrophysical Journal*, 857, 17, doi: [10.3847/1538-4357/aab3d5](https://doi.org/10.3847/1538-4357/aab3d5)
- Mancini, C., Daddi, E., Juneau, S., et al. 2019, *MNRAS*, 489, 1265, doi: [10.1093/mnras/stz2130](https://doi.org/10.1093/mnras/stz2130)
- Maragkoudakis, A., Zezas, A., Ashby, M. L. N., & Willner, S. P. 2016, *MNRAS*, 466, 1192, doi: [10.1093/mnras/stw3180](https://doi.org/10.1093/mnras/stw3180)
- Marinacci, F., Vogelsberger, M., Pakmor, R., et al. 2018, *MNRAS*, 480, 5113, doi: [10.1093/mnras/sty2206](https://doi.org/10.1093/mnras/sty2206)
- McDonough, B. 2025, Software: ScaleRPy, 1.1.1, Zenodo, doi: [10.5281/zenodo.15047562](https://doi.org/10.5281/zenodo.15047562)
- McDonough, B., Curtis, O., & Brainerd, T. G. 2023, *ApJ*, 958, 19, doi: [10.3847/1538-4357/acef0b](https://doi.org/10.3847/1538-4357/acef0b)
- McDonough, B., Curtis, O., & Brainerd, T. G. 2025, *ApJ*, 978, 67
- Medling, A. M., Cortese, L., Croom, S. M., et al. 2018, *MNRAS*, 475, 5194, doi: [10.1093/mnras/sty127](https://doi.org/10.1093/mnras/sty127)
- Naiman, J. P., Pillepich, A., Springel, V., et al. 2018, *MNRAS*, 477, 1206, doi: [10.1093/mnras/sty618](https://doi.org/10.1093/mnras/sty618)
- Nelson, D., Pillepich, A., Springel, V., et al. 2018, *MNRAS*, 475, 624, doi: [10.1093/mnras/stx3040](https://doi.org/10.1093/mnras/stx3040)
- Nelson, D., Springel, V., Pillepich, A., et al. 2019, *Comput. Astrophys.*, 6, 2
- Pessa, I., Schinnerer, E., Belfiore, F., et al. 2021, *A&A*, 650, A134, doi: [10.1051/0004-6361/202140733](https://doi.org/10.1051/0004-6361/202140733)
- Pillepich, A., Nelson, D., Hernquist, L., et al. 2018, *MNRAS*, 475, 648, doi: [10.1093/mnras/stx3112](https://doi.org/10.1093/mnras/stx3112)
- Planck Collaboration. 2016, *A&A*, 594, A13
- Popesso, P., Concas, A., Morselli, L., et al. 2019, *MNRAS*, 483, 3213, doi: [10.1093/mnras/sty3210](https://doi.org/10.1093/mnras/sty3210)
- Renzini, A., & Peng, Y.-j. 2015, *ApJL*, 801, L29, doi: [10.1088/2041-8205/801/2/L29](https://doi.org/10.1088/2041-8205/801/2/L29)
- Scott, D. W. 1992, *Multivariate density estimation*, Wiley Series in Probability and Statistics (Nashville, TN: John Wiley & Sons)
- Springel, V., Pakmor, R., Pillepich, A., et al. 2018, *MNRAS*, 475, 676, doi: [10.1093/mnras/stx3304](https://doi.org/10.1093/mnras/stx3304)
- Trayford, J. W., & Schaye, J. 2019, *MNRAS*, 485, 5715, doi: [10.1093/mnras/stz757](https://doi.org/10.1093/mnras/stz757)
- Virtanen, P., Gommers, R., Oliphant, T. E., et al. 2020, *Nature Methods*, 17, 261, doi: [10.1038/s41592-019-0686-2](https://doi.org/10.1038/s41592-019-0686-2)
- Wetzel, A., Hayward, C. C., Sanderson, R. E., et al. 2023, *ApJS*, 265, 44, doi: [10.3847/1538-4365/acb99a](https://doi.org/10.3847/1538-4365/acb99a)